

## A mass model for the lensing cluster SDSS J1004+4112: constraints from the fourth time delay

R. FORÉS-TORIBIO,<sup>1,2</sup> J. A. MUÑOZ,<sup>1,2</sup> C. S. KOCHANEK,<sup>3,4</sup> AND E. MEDIAVILLA<sup>5,6</sup>

<sup>1</sup>*Departamento de Astronomía y Astrofísica, Universidad de Valencia, E-46100 Burjassot, Valencia, Spain*

<sup>2</sup>*Observatorio Astronómico, Universidad de Valencia, E-46980 Paterna, Valencia, Spain*

<sup>3</sup>*Department of Astronomy, The Ohio State University, 140 West 18th Avenue, Columbus, OH 43210, USA*

<sup>4</sup>*Center for Cosmology and Astroparticle Physics, The Ohio State University, 191 West Woodruff Avenue, Columbus, OH 43210, USA*

<sup>5</sup>*Instituto de Astrofísica de Canarias, Vía Láctea S/N, La Laguna, E-38205, Tenerife, Spain*

<sup>6</sup>*Departamento de Astrofísica, Universidad de la Laguna, Tenerife, Spain*

### ABSTRACT

We have built a new model for the lens SDSS J1004+4112 including the recently measured time delay of the fourth quasar image. This time delay has a strong influence on the inner mass distribution of the lensing cluster ( $\rho \propto r^{-\alpha}$ ) allowing us to determine  $\alpha = 1.18_{-0.03(-0.18)}^{+0.02(+0.11)}$  at 68% (95%) confidence level in agreement with hydrodynamical simulations of massive galaxy clusters. We find an offset between the brightest cluster galaxy (BCG) and the dark matter halo of  $3.8_{-0.7(-1.3)}^{+0.6(+1.4)}$  kpc at 68% (95%) confidence which is compatible with other galaxy cluster measurements. As an observational challenge, the estimated time delay between the leading image C and the faint (I=24.7) fifth image E is roughly 8 years.

*Keywords:* Gravitational lensing (670): Strong gravitational lensing (1643) — Galaxy clusters (584) — Dark matter distribution (356) — Quasars (1319): individual: SDSS J1004+4112

### 1. INTRODUCTION

The lens system SDSS J1004+4112 was the first example of a quasar lensed by a cluster (Inada et al. 2003). The source and lens redshifts are  $z_s = 1.73$  and  $z_l = 0.68$ , respectively. This leads to an image separation of  $15''$  and large magnified images of the host galaxy. It is the second largest quasar lens after SDSS J1029+2623 (Inada et al. 2006).

Since its discovery, many additional observational constraints have been obtained: more galaxy cluster members (Oguri et al. 2004), the central quasar image (Inada et al. 2005, 2008), other background lensed sources (Sharon et al. 2005; Liesenborgs et al. 2009; Oguri 2010), the velocity dispersion of the brightest galaxy cluster (Inada et al. 2008) and the time delays between quasar images A, B and C (Fohlmeister et al. 2007, 2008).

As new observational constraints were measured, increasingly sophisticated mass models of the lens cluster were made using both parametric (Inada et al. 2003; Oguri et al. 2004; Fohlmeister et al. 2007; Oguri 2010) and non-parametric (Williams & Saha 2004; Saha et al. 2006; Liesenborgs et al. 2009; Mohammed et al. 2015) approaches. Recently, the time delay of the fourth quasar image (Muñoz et al. 2022) has been measured at 2457 days between images D and C, and it is over one

year longer than predicted (Oguri 2010). Indeed, the ability of the models to predict the unmeasured time delays has been remarkably poor.

Apart from the models of the mass distribution, this system has been widely studied not only in the optical but also from X-rays to radio (Lamer et al. 2006; Ota et al. 2006; Ross et al. 2009; Jackson 2011; Chen et al. 2012; McKean et al. 2021). However, there are still issues that remain unsolved like the origin of the enhanced asymmetric wings in the broad emission lines of quasar image A (Richards et al. 2004; Gómez-Álvarez et al. 2006; Lamer et al. 2006; Motta et al. 2012; Fian et al. 2018, 2021; Popović et al. 2020).

Here we revisit the mass model making use of the newly measured time delay. The new delay should help to constrain the inner mass profile of the cluster halo and to look for deviations from an NFW profile (Kawano & Oguri 2006; Oguri 2010). The paper is organized as follows. In Section 2 we present the available observational constraints. In Section 3 we describe the modelling method and the components of the mass model. Section 4 presents the results and they are discussed in Section 5. Throughout this paper we assume a flat  $\Lambda$ CDM cosmology with  $\Omega_M = 0.26$ ,  $\Omega_\Lambda = 0.74$  and  $H_0 = 72$  km/s Mpc<sup>-1</sup>.

## 2. OBSERVATIONAL DATA

In addition to the lensed quasar, SDSS J1004+4112 has 7 lensed background galaxies at 3 different redshifts. Their redshifts, image positions and magnitudes (with respect to quasar image A) are from Oguri (2010) and listed in Table 1. For the quasar time delays we use the results of Muñoz et al. (2022) with the uncertainties set to 5 times the formal errors (see Table 1) since time delay uncertainties are almost always underestimated (see, e.g., Tie & Kochanek 2018). We also adopted the positions, ellipticities, position angles and luminosity ratios (with respect to the central galaxy) of 14 cluster galaxy members (see Table 2) from Oguri (2010). For the brightest cluster galaxy (BCG) we adopt a position of ( $7''114, 4''409$ ), ellipticity  $e = 0.30 \pm 0.05$ , major axis PA  $\theta_e = 152 \pm 5^\circ$  (Oguri 2010) and a central velocity dispersion of  $352 \pm 13$  km/s (Inada et al. 2008).

## 3. SYSTEM MODELLING

We modelled the mass distribution of the lens using both *lensmodel* (Keeton 2001) and *glafic* (Oguri 2010). Both packages employ parametrized mass profiles. The final results are computed with *glafic* in order to ease the comparison with Oguri (2010). The different mass components and any constraints on their properties are described in the following subsections.

### 3.1. Dark matter halo

We modelled the dark matter mass distribution as a generalized Navarro-Frenk-White (gNFW) profile (Navarro et al. 1997; Jing & Suto 2000) with the 3D density profile

$$\rho = \frac{\rho_s}{(r/r_s)^\alpha (1 + r/r_s)^{3-\alpha}}. \quad (1)$$

With the addition of its 2D ellipticity, the projected profile is completely described by 7 parameters:  $M_{vir}$  (virial mass),  $x$  and  $y$  (position),  $e$  (ellipticity),  $\theta_e$  (position angle),  $c_{-2}$  (concentration parameter) and  $\alpha$  (inner slope). The relationships between  $(\rho_r, r_s)$  and  $(M_{vir}, c_{-2})$  can be found in *glafic*'s manual<sup>1</sup>. We do not impose any restrictions on the parameters, however the inner slope  $\alpha$  is set to unity until the whole model is optimized.

### 3.2. Brightest cluster galaxy

The BCG is parametrized by a pseudo-Jaffe (pJaffe) profile

$$\kappa = 2\pi \left(\frac{\sigma}{c}\right)^2 \frac{D_{ls}}{D_{os}} \left[ \frac{1}{R} - \frac{1}{\sqrt{r_{trun}^2 + R^2}} \right]. \quad (2)$$

<sup>1</sup> Available at <https://www.slac.stanford.edu/~oguri/glafic/index.v1.html>

**Table 1.** Redshift, positions, magnitudes and time delays for the observed images of the lensed sources

Name	$z_s$	$x$ (")	$y$ (")	$\Delta m$	$\Delta t$ (days)
QSO.A		0.000	0.000	$\equiv 0$	$825.99 \pm 2.10$
QSO.B		-1.317	3.532	$0.35 \pm 0.30$	$781.92 \pm 2.20$
QSO.C	1.734	11.039	-4.492	$0.87 \pm 0.30$	$\equiv 0$
QSO.D		8.399	9.707	$1.50 \pm 0.30$	$2456.99 \pm 5.55$
QSO.E		7.197	4.603	$6.3 \pm 0.8$	...
A1.1		3.93	-2.78	...	...
A1.2		1.33	19.37	...	...
A1.3	3.33	19.23	14.67	...	...
A1.4		18.83	15.87	...	...
A1.5		6.83	3.22	...	...
A2.1		4.13	-2.68	...	...
A2.2		1.93	19.87	...	...
A2.3	3.33	19.43	14.02	...	...
A2.4		18.33	15.72	...	...
A2.5		6.83	3.12	...	...
A3.1		4.33	-1.98	...	...
A3.2		2.73	20.37	...	...
A3.3	3.33	19.95	13.04	...	...
A3.4		18.03	15.87	...	...
A3.5		6.83	3.02	...	...
B1.1		8.88	-2.16	...	...
B1.2	2.74	-5.45	15.84	...	...
B1.3		8.33	2.57	...	...
B2.1		8.45	-2.26	...	...
B2.2	2.74	-5.07	16.04	...	...
B2.3		8.33	2.57	...	...
C1.1		10.25	-3.06	...	...
C1.2	3.28	-7.55	15.39	...	...
C1.3		8.49	2.72	...	...
C2.1		9.95	-3.36	...	...
C2.2	3.28	-7.30	15.44	...	...
C2.3		8.49	2.72	...	...

NOTE—The position errors adopted for the QSO are  $0.04''$  whereas for the galaxies are  $0.4''$ .

This model is defined by 6 parameters when ellipticity is added:  $\sigma$  (velocity dispersion),  $x$  and  $y$  (position),  $e$  (ellipticity),  $\theta_e$  (position angle) and  $r_{trun}$  (truncation radius, beyond this scale, the convergence falls as  $R^{-3}$ ). We fix the position to the observed value and include Gaussian priors on  $e$  and  $\theta_e$ . The observed velocity dispersion does not directly correspond to the model dispersion and Appendix A details how we use the measured dispersion as a constraint to obtain a model velocity dispersion prior of  $325 \pm 20$  km/s. The truncation radius is loosely constrained using the same prior as Oguri (2010) ( $r_{trun} = 8'' \pm 4''$ ) because of the observed corre-

**Table 2.** Positions, ellipticities, position angles and luminosity ratios of 14 cluster galaxy members

x (")	y (")	e	PA (°)	L/L <sub>BCG</sub>
30.78	4.50	0.2723	-2.90	0.5050
12.14	3.67	0.2426	-131.80	0.2970
2.76	14.13	0.1077	-161.50	0.2250
25.29	-9.06	0.1028	-70.00	0.0950
-9.22	-2.53	0.0885	-42.80	0.1510
14.54	24.23	0.0461	-82.00	0.1830
24.61	4.72	0.0433	-60.40	0.1720
9.36	2.41	0.2249	-100.30	0.4060
2.767	-0.171	0.0517	-21.8	0.238
14.789	-5.454	0.0453	-127.7	0.41
-1.359	0.482	0.0224	51.3	0.21
12.00	13.82	0.0711	-92.7	0.368
7.84	9.10	0.0118	-17.0	0.10
-7.21	-8.84	0.0661	-139.6	0.450

lation between velocity dispersion and truncation radius (Natarajan et al. 2009).

### 3.3. Other cluster galaxy members

The rest of the cluster galaxies are modelled by scaled pseudo-Jaffe ellipsoids (mass profile ‘gals’ in the *glafic* software). Their  $\sigma$  and  $r_{trun}$  are scaled relative to the luminosity of the BCG as

$$\sigma = \sigma_* \left( \frac{L}{L_*} \right)^{1/4} \quad \text{and} \quad r_{trun} = r_* \left( \frac{L}{L_*} \right)^{1/2} \quad (3)$$

where  $\sigma_*$  and  $r_*$  are model parameters. The ratio  $L/L_*$ , ellipticity and position angle of each galaxy member is constrained by the observed values given in Table 2. Since the reference galaxy is the BCG, the scale parameters  $\sigma_*$  and  $r_*$  are initially set equal to the velocity dispersion and truncation radius of the BCG but, during the optimization, both are allowed to vary.

### 3.4. External perturbations

We also include multipole perturbations of order  $m=2,3,4,5$  (mpoles model) with the potential

$$\phi = -\frac{\epsilon}{m} r^2 \cos m(\theta - \theta_\epsilon - \pi/2). \quad (4)$$

For  $m=2$ , the perturbation is an external shear (named ‘pert’ in *glafic*) so we denote the  $m=2$  parameters as  $\gamma$  and  $\theta_\gamma$  instead. We center these potentials on the position of the DM halo.

### 3.5. Background sources

At higher redshift than the quasar there are three groups of galaxies (A, B and C) at different redshifts. Group A is composed of three galaxies each lensed into five images. Groups B and C each have two galaxies and each is split into three images. The observed positions of these images along with their redshifts and magnitudes are also given in Table 1. All the background sources are modelled as point sources with fixed redshift so the fit parameters are their unlensed positions.

In total we have 77 observational constraints and 37 model parameters leaving us with  $\nu=40$  degrees of freedom (dof).

## 4. RESULTS

The optimization was performed as follows. First we optimized all the parameters fitting the images on the source plane. Once we found the minimum  $\chi^2$ , we ran the optimization fitting the images on the image plane. Next we computed the parameter uncertainties fitting the images on the source plane in order to maintain a sensible computing time. Finally, we ran the optimization on the image plane using as initial parameters the model that produced the minimum  $\chi^2$  in the uncertainties estimation step.

The central values and the 1- $\sigma$  and 2- $\sigma$  (corresponding to  $\Delta\chi^2 = 1$  and  $\Delta\chi^2 = 4$ , respectively) uncertainties are given in Table 3 and the  $\chi^2$  profiles for each parameter are displayed in Figure 1. The mass, concentration and inner slope of the gNFW profile do not have smooth  $\chi^2$  profiles, especially for the inner slope  $\alpha$ . These parameters are correlated and the minimizer has difficulties in finding the true minimum. We define the uncertainties using the model most distant from the minimum that is within the  $\Delta\chi^2$  limit.

The optimization on the image plane starting from the parameters which give the minimum  $\chi^2$  in the error computations is considered the best fit model and it is shown in the last column of Table 3. The central values of the  $\chi^2$  profiles do not exactly correspond to the best fit parameters (see columns 3 and 6 of Table 3) because the two results come from different optimization procedures. Nonetheless, all the parameters of the best model fit lie between the reported 1- $\sigma$  confidence intervals except for  $\sigma$  and  $\sigma_*$  which lie between their 2- $\sigma$  intervals.

The predicted images positions and critical curves of the four background sources for this model are shown in Figure 2. This best fit model has a  $\chi^2$  value of 59.91 in the image plane which corresponds to  $\chi^2_\nu = \chi^2/\nu = 1.50$ . The observational constraints on the quasar contribute

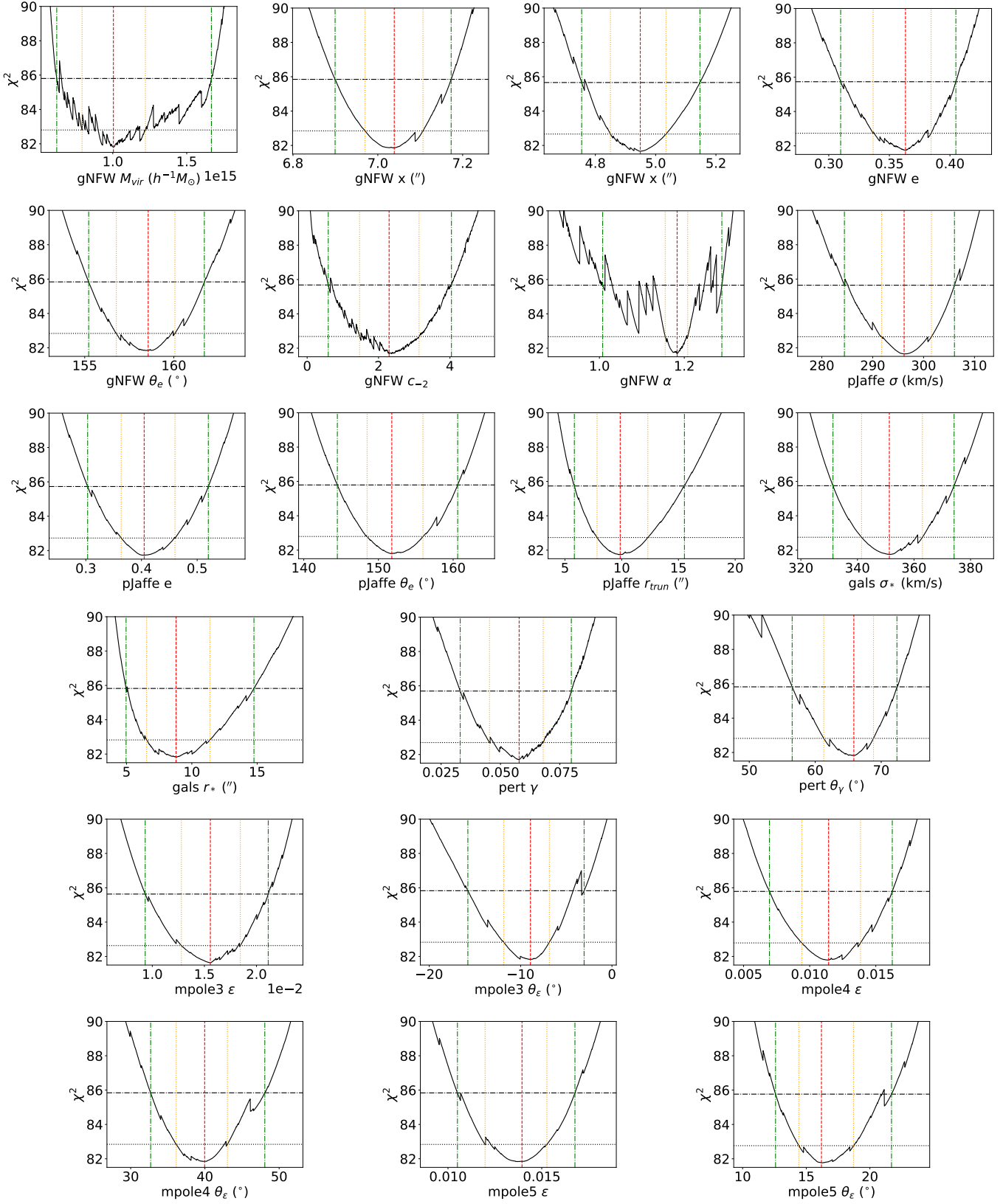


**Figure 1.**  $\chi^2$  profiles for each model parameter. Red dashed lines mark the values for which the  $\chi^2$  is minimized, orange dotted lines are the  $1\text{-}\sigma$  errors and green dash-dotted lines are the  $2\text{-}\sigma$  errors.

**Table 3.** Central values and errors at 1- $\sigma$  and 2- $\sigma$  for the mass model parameters

Model	Parameters		1- $\sigma$	2- $\sigma$	Best fit
gNFW	$M_{vir}$ ( $10^{15}h^{-1}M_{\odot}$ )	1.0	+0.2 -0.2	+0.7 -0.4	1.0
	x (")	7.04	+0.07 -0.07	+0.13 -0.14	7.03
	y (")	4.95	+0.09 -0.10	+0.2 -0.19	4.88
	e	0.36	+0.02 -0.03	+0.04 -0.05	0.36
	$\theta_e$ ( $^{\circ}$ )	158.6	+1.5 -1.8	+3 -3	158.1
	$c_{-2}$	2.3	+0.8 -0.8	+1.7 -1.7	2.2
	$\alpha$	1.18	+0.02 -0.03	+0.11 -0.18	1.20
pJaffe	$\sigma$ (km/s)	296	+5 -4	+10 -12	290
	e	0.40	+0.06 -0.04	+0.12 -0.10	0.37
	$\theta_e$ ( $^{\circ}$ )	152	+4 -3	+9 -7	154
	$r_{trun}$ (")	10	+2 -2	+6 -4	10
gals	$\sigma_*$ (km/s)	351	+12 -10	+20 -20	337
	$r_*$ (")	9	+3 -2	+6 -4	9
pert	$\gamma$ ( $10^{-2}$ )	5.8	+1.0 -1.2	+2 -2	5.7
	$\theta_{\gamma}$ ( $^{\circ}$ )	66	+3 -5	+7 -9	65
mpole3	$\epsilon$ ( $10^{-2}$ )	1.6	+0.3 -0.3	+0.6 -0.6	1.4
	$\theta_{\epsilon}$ ( $^{\circ}$ )	-9	+2 -3	+6 -7	-7
mpole4	$\epsilon$ ( $10^{-2}$ )	1.1	+0.2 -0.2	+0.5 -0.4	1.1
	$\theta_{\epsilon}$ ( $^{\circ}$ )	40	+3 -4	+8 -7	41
mpole5	$\epsilon$ ( $10^{-2}$ )	1.39	+0.13 -0.2	+0.3 -0.3	1.25
	$\theta_{\epsilon}$ ( $^{\circ}$ )	16.2	+2 -1.8	+6 -4	17.6

**Table 4.** Convergence  $\kappa$ , shear  $\gamma$  and magnification  $\mu$  at the quasar images positions

Quasar image	$\kappa$	$\gamma$	$\mu$
A	0.728940	0.333242	-26.612171
B	0.650724	0.232737	14.743285
C	0.587686	0.225075	8.379131
D	1.015191	0.489943	-4.169912
E	5.669724	3.622670	0.115173

11.76 to the total  $\chi^2$  and the A, B and C groups of galaxies contribute 30.95, 2.92 and 8.16, respectively. Additionally, the  $\chi^2$  associated with the 6 parameter priors is 6.13. The model fits all 3 delays well, with a  $\chi^2=1.33$  for the delay constraints. The model predicts a time delay between the leading image C and the fifth image E of  $\Delta t_{EC}=2853.90$  days or 7.81 years, although this delay will be virtually impossible to measure due to the faintness of image E. Additionally, Table 4 gives the convergence  $\kappa$  and shear  $\gamma$  at the quasar positions along with the total magnification.

The goodness of the fit for the A group of galaxies is substantially worse than for the rest of the background galaxies because the model predicts 7 images instead of the 5 observationally reported. This occurs because the images A1.2, A2.2 and A3.2 lie very close to a critical curve. A very small change in the source position can change the number of the images and that is precisely what occurred in our model where one image has unfolded into three (they are marked as ‘unfolded’ in Figure 2). The A group images are really composed of extended arcs, so the model would be more realistic if we modelled the galaxies as extended sources. Despite that, the reconstructed image positions properly reproduce all the main structures of the system (see Figure 3).

## 5. DISCUSSION AND CONCLUSIONS

One of the main results from our model is the value of the inner slope of the generalized NFW profile,  $\alpha = 1.18_{-0.03}^{+0.02(+0.11)}$  at the 68% (95%) confidence level. We must bear in mind that this value is the asymptotic slope of the dark matter halo for  $r \rightarrow 0$ . However at this regime the mass of the BCG becomes important and it is difficult to distinguish both components because the lensing effect is sensitive to the total mass of the system. A different parametrization of the BCG would alter the inner slope value of the generalized NFW profile. If we wanted to determine the mass distribution in the innermost regions of the cluster more precisely, we would probably need a velocity dispersion profile in order to better separate the two components.

Newman et al. (2013a,b) made such models for 7 massive galaxy clusters and found very shallow inner slopes of  $0.50 \pm 0.10(\text{random})_{-0.13}^{+0.14}(\text{systematic})$ . On the other hand, Smith et al. (2017) inferred a DM inner slope for the cluster Abell 1201 of  $\alpha = 1.01 \pm 0.12$  using the same procedure but with other assumptions. Schaller et al. (2015) and He et al. (2020) tested this method with the EAGLE hydrodynamical simulations and found that the results were dependent on the assumptions about the mass-to-light ratio and the intrinsic degeneracies of the profiles. The simulations suggest that the dark matter halo distribution is compatible with the original NFW profile and our value. While our model likely has degeneracies between the inner slope of the BCG (which we hold fixed) and the DM halo, our result is compatible with these simulations of massive galaxy clusters.

Our inferred virial mass and concentration parameter for the generalized NFW cluster halo are in good agreement with those obtained in the lens model of Oguri (2010). However they differ from the values reported by Ota et al. (2006) based on X-ray observations,

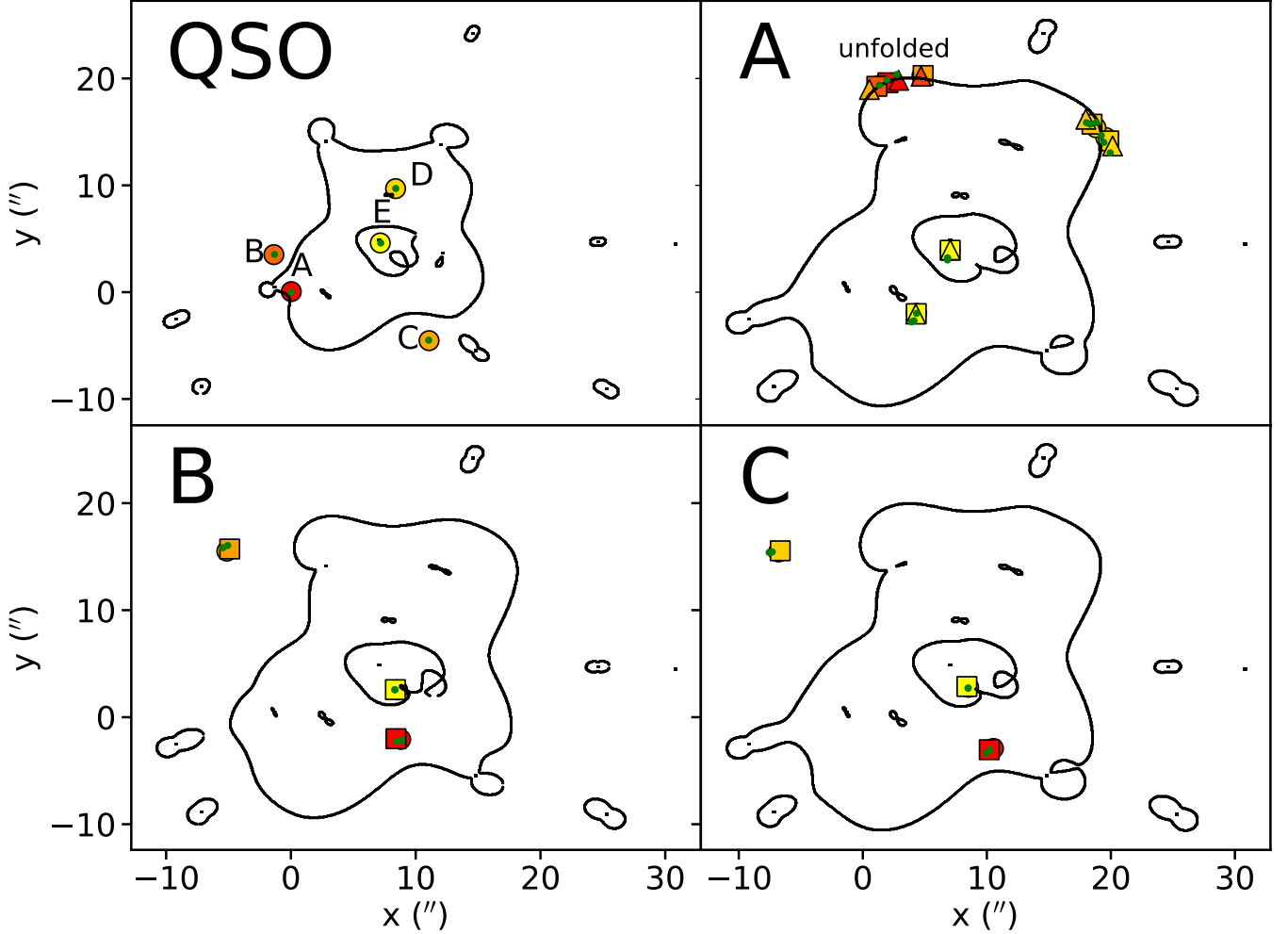


**Figure 2.** Critical curves and images positions for the four background sources. The green dots mark the observed positions of the images. Circles denote the quasar, A1, B1 and C1 images, squares represent the images of A2, B2 and C2 and lastly the triangles mark A3 images. Additionally, images are color coded depending on their flux, from the brightest in red to the dimmest in yellow.

$M_{vir} = 4.2_{-1.5}^{+2.6} \times 10^{14} h^{-1} M_{\odot}$  and  $c_{-2} = 6.1_{-1.2}^{+1.5}$ . These differences can be explained by the degeneracy between  $M_{vir}$ ,  $c_{-2}$  and  $\alpha$  in strong lensing models pointed out by Oguri (2010). The source of this degeneracy comes from the fact that the lensing effect is mainly sensitive to the enclosed mass projected inside the region delimited by the lensed images but the parameters  $M_{vir}$  and  $c_{-2}$  are defined on the much larger scale of the virial radius and so are extrapolations of our mass model. In this system, the outermost images are  $\sim 125$  kpc from the center of the cluster whereas the parameters  $M_{vir}$  and  $c_{-2}$  are extrapolations to a radius  $r_{vir} \approx 2$  Mpc. It is better to test the compatibility of the two results by comparing the mass enclosed inside a smaller radius to which both methods are sensitive. Ota et al. (2006) reported the projected mass inside  $70 h^{-1} \text{kpc}$  to

be  $3.5_{-0.8}^{+1.3} \times 10^{13} h^{-1} M_{\odot}$ . In good agreement with our enclosed mass of  $3.7 \times 10^{13} h^{-1} M_{\odot}$ .

We find an offset between the BCG and the dark matter halo of  $3.8_{-0.7}^{+0.6(+1.4)}$  kpc at the 68% (95%) confidence level. Previous parametric models have found similar offsets for this system (Oguri et al. 2004; Fohlmeister et al. 2007) although Oguri (2010) found an offset compatible with zero. From fitting 10000 galaxy clusters with strong lensing measurements, Zitrin et al. (2012) found a mean separation of  $18_{-12}^{+37}$  kpc where the uncertainty is the observed scatter. Kluge et al. (2020) estimated the separation between the BCG and the intracluster light (ICL) tracing the dark matter distribution for local clusters, and found a mean offset of 36 kpc with a sample scatter of 33 kpc. Our inferred offset is compatible with both results.

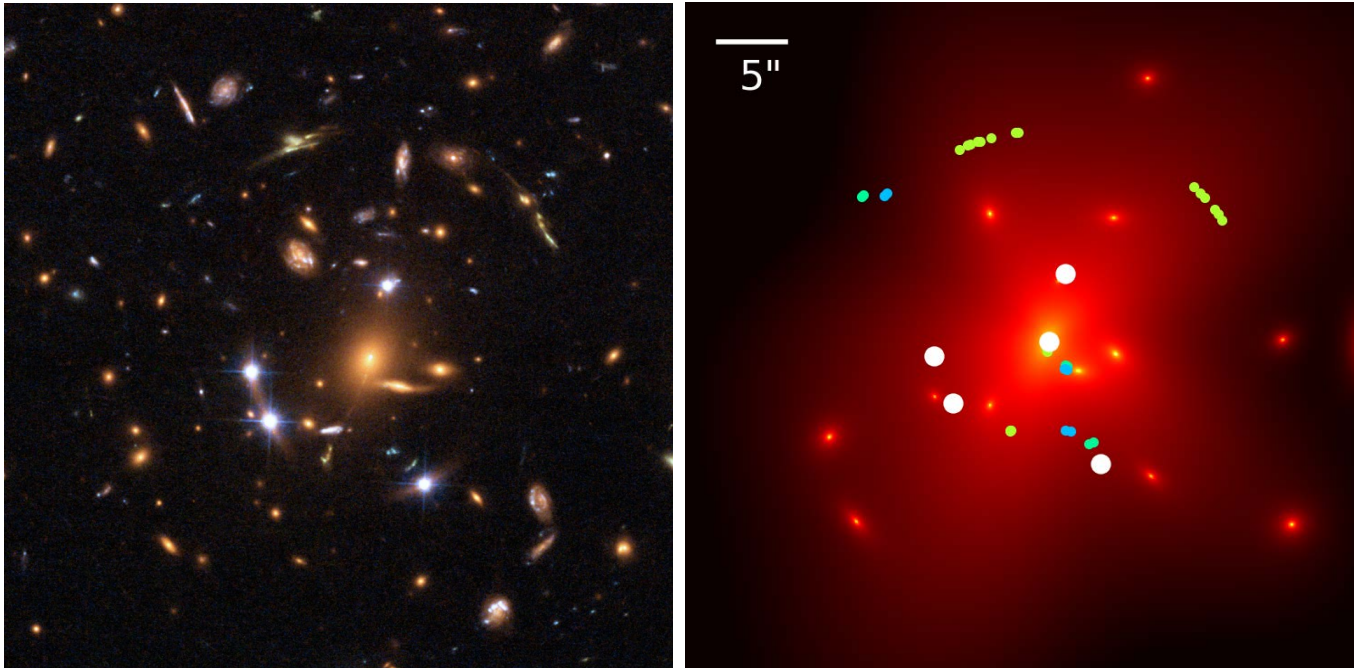


**Figure 3.** The left panel shows the HST ACS/WFC (GO-9744, PI: C. Kochanek) images of the lens. The right panel shows the reconstructed mass distribution on a logarithmic scale along with the images positions: quasar in white and galaxy group A in lime-green, B in blue and C in turquoise. The orientation for both figures is North up, West right.

We also find that the DM halo and the BCG are virtually aligned and with similar ellipticities. On the other hand, the velocity dispersion scale parameter for the cluster galaxy members differs from the BCG parametrization even though they were started with values scaled to the BCG. This difference suggests that BCGs are structurally different from the other cluster galaxy members because they have more DM content than the rest. Another feature in the BCG velocity dispersion is that the model fits the pseudo-Jaffe velocity dispersion to a smaller value than the prior. That could be explained by the fact that the observed velocity dispersion includes the effect of the dark matter halo whereas the model velocity dispersion parameter represents only the mass of the BCG.

In conclusion, we have made use of the recently measured time delay of image D and previous observational

data to model the lensing cluster SDSS J1004+4112. The model parameters we obtained are broadly consistent with previous estimates but they are now better constrained, in particular the inner slope of the dark matter halo of the lensing cluster.

This research is based on observations made with the NASA/ESA Hubble Space Telescope obtained from the Space Telescope Science Institute, which is operated by the Association of Universities for Research in Astronomy, Inc., under NASA contract NAS 5-26555. These observations are associated with program GO-9744. JAM and EM are supported by the Spanish Ministerio de Ciencia e Innovación with the grants PID2020-118687GB-C32 and PID2020-118687GB-C31. JAM is also supported by the Generalitat Valenciana with the project of excellence Prometeo/2020/085. CSK is supported by NSF grants AST-1908570 and AST-1814440.

## APPENDIX

### A. MODEL AND OBSERVED VELOCITY DISPERSIONS

The *glafic* package parametrizes the pseudo-Jaffe profile with a velocity dispersion which corresponds to the central velocity dispersion of a Singular Isothermal Sphere ( $\sigma_{mod}$ ). On the other hand, the observed velocity dispersion is the averaged velocity dispersion ( $\sigma_{obs}$ ) along the line of sight inside a finite size slit. The observed velocity dispersion is produced by a combination of the BCG mass and the dark matter halo, however we assume that the dark matter halo

is negligible for a central velocity dispersion and we only consider the dispersion velocity due to the BCG modelled as a pseudo-Jaffe ellipsoid. In order to obtain their relationship we make use of the expressions of densities, masses and velocities dispersion of [Elíasdóttir et al. \(2007\)](#). Additionally, we transform the expressions into dimensionless quantities plus a prefactor in order to simplify the expressions and we end with the following definitions:

- Surface density:

$$\Sigma(R) = \frac{\sigma_{mod}^2}{2Gr_{trun}} \tilde{\Sigma}(x) \quad \text{where} \quad \tilde{\Sigma}(x) = \frac{1}{\sqrt{f^2 + x^2}} - \frac{1}{\sqrt{1 + x^2}} \quad (\text{A1})$$

- Volume density:

$$\rho(r) = \frac{\sqrt{q}(1-f^2)\sigma_{mod}^2}{2\pi Gr_{trun}^2} \tilde{\rho}(z) \quad \text{where} \quad \tilde{\rho}(z) = \frac{1}{(f^2 + z^2)(1 + z^2)} \quad (\text{A2})$$

- Enclosed projected mass:

$$M_{2D}(R) = \frac{\pi r_{trun} \sigma_{mod}^2}{Gq} \tilde{M}_{2D}(x) \quad \text{where} \quad \tilde{M}_{2D}(x) = \sqrt{f^2 + x^2} - \sqrt{1 + x^2} + 1 - f \quad (\text{A3})$$

- Enclosed mass:

$$M_{3D}(r) = \frac{2r_{trun} \sigma_{mod}^2}{Gq} \tilde{M}_{3D}(z) \quad \text{where} \quad \tilde{M}_{3D}(z) = \arctan(z) - f \arctan(z/f) \quad (\text{A4})$$

- Projected velocity dispersion:

$$\sigma_P^2(R) = \frac{4(1-f^2)\sigma_{mod}^2}{\pi\sqrt{q}} \tilde{\sigma}_P^2(x) \quad \text{where} \quad \tilde{\sigma}_P^2(x) = \frac{1}{\tilde{\Sigma}(x)} \int_x^\infty \frac{\tilde{M}_{3D}(z)\tilde{\rho}(z)}{z^2} \sqrt{z^2 - x^2} dz \quad (\text{A5})$$

- Averaged projected velocity dispersion inside R:

$$\sigma_{obs}^2 = \langle \sigma_P^2 \rangle (R) = \frac{4(1-f^2)\sigma_{mod}^2}{\pi\sqrt{q}} \langle \tilde{\sigma}_P^2 \rangle (x) \quad \text{where} \quad \langle \tilde{\sigma}_P^2 \rangle (x) = \frac{1}{\tilde{M}_{2D}(x)} \int_0^x \tilde{\sigma}_P^2(x') \tilde{\Sigma}(x') x' dx' \quad (\text{A6})$$

The dimensionless variables are  $x \equiv R\sqrt{q}/r_{trun}$ ,  $z \equiv r\sqrt{q}/r_{trun}$ ,  $f \equiv r_{core}/r_{trun}$  and  $q = 1 - e$  is the axis ratio. In our case,  $f = 0$  and the slit width employed to measure the velocity dispersion was  $0''.4$  ([Inada et al. 2008](#)) so we used the average dispersion inside  $R=0''.2$ . Taking into account the central values and errors for the ellipticity and the truncation radius, we obtain  $\sigma_{mod,prior} = 325 \pm 20$  km/s as the prior for the model velocity dispersion.

## REFERENCES

- Chen, B., Dai, X., Kochanek, C. S., et al. 2012, *ApJ*, 755, 24
- Elíasdóttir, Á., Limousin, M., Richard, J., et al. 2007, arXiv:0710.5636
- Fian, C., Guerras, E., Mediavilla, E., et al. 2018, *ApJ*, 859, 50
- Fian, C., Mediavilla, E., Motta, V., et al. 2021, *A&A*, 653, A109
- Fohlmeister, J., Kochanek, C. S., Falco, E. E., et al. 2007, *ApJ*, 662, 62
- Fohlmeister, J., Kochanek, C. S., Falco, E. E., et al. 2008, *ApJ*, 676, 761
- Gómez-Álvarez, P., Mediavilla, E., Muñoz, J. A., et al. 2006, *ApJL*, 645, L5
- He, Q., Li, H., Li, R., et al. 2020, *MNRAS*, 496, 4717
- Inada, N., Oguri, M., Pindor, B., et al. 2003, *Nature*, 426, 810
- Inada, N., Oguri, M., Keeton, C. R., et al. 2005, *PASJ*, 57, L7
- Inada, N., Oguri, M., Morokuma, T., et al. 2006, *ApJL*, 653, L97
- Inada, N., Oguri, M., Falco, E. E., et al. 2008, *PASJ*, 60, 27
- Jackson, N. 2011, *ApJL*, 739, L28
- Jing, Y. P. & Suto, Y. 2000, *ApJL*, 529, L69
- Kawano, Y. & Oguri, M. 2006, *PASJ*, 58, 271

- Keeton, C. R. 2001, astro-ph/0102340
- Kluge, M., Neureiter, B., Riffeser, A., et al. 2020, ApJS, 247, 43
- Lamer, G., Schwobe, A., Wisotzki, L., et al. 2006, A&A, 454, 493
- Liesenborgs, J., de Rijcke, S., Dejonghe, H., et al. 2009, MNRAS, 397, 341
- McKean, J. P., Luichies, R., Drabent, A., et al. 2021, MNRAS, 505, L36
- Mohammed, I., Saha, P., & Liesenborgs, J. 2015, PASJ, 67, 21
- Motta, V., Mediavilla, E., Falco, E., et al. 2012, ApJ, 755, 82
- Muñoz, J., Kochanek, C., Fohlmeister, J., et al. 2022 ApJ, submitted, arXiv:2206.08597
- Natarajan, P., Kneib, J.-P., Smail, I., et al. 2009, ApJ, 693, 970
- Navarro, J. F., Frenk, C. S., & White, S. D. M. 1997, ApJ, 490, 493
- Newman, A. B., Treu, T., Ellis, R. S., et al. 2013, ApJ, 765, 24
- Newman, A. B., Treu, T., Ellis, R. S., et al. 2013, ApJ, 765, 25
- Oguri, M., Inada, N., Keeton, C. R., et al. 2004, ApJ, 605, 78
- Oguri, M. 2010, PASJ, 62, 1017
- Ota, N., Inada, N., Oguri, M., et al. 2006, ApJ, 647, 215
- Popović, L. Č., Afanasiev, V. L., Moiseev, A., et al. 2020, A&A, 634, A27
- Richards, G. T., Keeton, C. R., Pindor, B., et al. 2004, ApJ, 610, 679
- Ross, N. R., Assef, R. J., Kochanek, C. S., et al. 2009, ApJ, 702, 472
- Saha, P., Read, J. I., & Williams, L. L. R. 2006, ApJL, 652, L5
- Schaller, M., Frenk, C. S., Bower, R. G., et al. 2015, MNRAS, 452, 343
- Sharon, K., Ofek, E. O., Smith, G. P., et al. 2005, ApJL, 629, L73
- Smith, R. J., Lucey, J. R., & Edge, A. C. 2017, MNRAS, 471, 383
- Tie, S. S. & Kochanek, C. S. 2018, MNRAS, 473, 80
- Williams, L. L. R. & Saha, P. 2004, AJ, 128, 2631
- Zitrin, A., Bartelmann, M., Umetsu, K., et al. 2012, MNRAS, 426, 2944